

Renormalization of the Gamow-Teller operator within the realistic shell modelL. Coraggio,¹ L. De Angelis,¹ T. Fukui,¹ A. Gargano,¹ N. Itaco,^{2,1} and F. Nowacki^{3,4,2}¹*Istituto Nazionale di Fisica Nucleare, Complesso Universitario di Monte S. Angelo, Via Cintia, I-80126 Napoli, Italy*²*Dipartimento di Matematica e Fisica, Università degli Studi della Campania “Luigi Vanvitelli”,
viale Abramo Lincoln 5, I-81100 Caserta, Italy*³*Université de Strasbourg, IPHC, 23 rue du Loess 67037 Strasbourg, France*⁴*CNRS, IPHC UMR 7178, 67037 Strasbourg, France*

(Received 11 December 2018; revised manuscript received 6 May 2019; published 23 July 2019)

In nuclear structure calculations, the choice of a limited model space, due to computational needs, leads to the necessity to renormalize the Hamiltonian as well as any transition operator. Here, we present a study of the renormalization procedure and effects of the Gamow-Teller operator within the framework of the realistic shell model. Our effective shell-model operators are obtained, starting from a realistic nucleon-nucleon potential, by way of the many-body perturbation theory in order to take into account the degrees of freedom that are not explicitly included in the chosen model space. The theoretical effective shell-model Hamiltonian and transition operators are then employed in shell-model calculations, whose results are compared with data of Gamow-Teller transition strengths and double- β half-lives for nuclei which are currently of interest for the detection of the neutrinoless double- β decay process, in a mass interval ranging from $A = 48$ up to $A = 136$. We show that effective operators are able to reproduce quantitatively the spectroscopic and decay properties without resorting to an empirical quenching neither of the axial coupling constant g_A , nor of the spin and orbital gyromagnetic factors. This should assess the reliability of applying present theoretical tools to this problematic.

DOI: [10.1103/PhysRevC.100.014316](https://doi.org/10.1103/PhysRevC.100.014316)**I. INTRODUCTION**

A longstanding issue of nuclear structure calculations is the need to reduce the number of the configurations available to the interacting nucleons, which constitute the nuclear system under investigation. Such approximations, that are necessary to overcome the computational complexity of the nuclear many-body problem, drive the nuclear structure practitioners to resort to effective Hamiltonians and operators, that depend on a certain set of parameters, built up to account for the degrees of freedom which do not appear explicitly in the calculated wave functions. The development of effective operators suitable to describe observables is a problem that has to be tackled in most nuclear structure models that relies on the truncation of the number of interacting nucleons and/or the dimension of the configuration space. This issue does not affect *ab initio* approaches when their results are convergent with respect to the truncation of the nuclear correlations that is needed to solve the many-body Schrödinger equation (see, for example, Ref. [1]).

In the nuclear shell model (SM), the physics of a certain nuclear system is described in terms only of a limited number of valence nucleons, that interact in a model space consisting of a major shell, placed outside a closed core made up by the remaining constituent nucleons, the latter being frozen inside a number of filled shells.

The status of the theoretical derivation of an effective shell-model Hamiltonian (H_{eff}), starting from a realistic nuclear potential, has reached notable progress nowadays, especially within the framework of the many-body perturbation

theory [2,3]. At present, realistic shell-model Hamiltonians are largely employed in shell-model calculations, exhibiting a substantial reliability (see, for example, Ref. [4] and references therein).

As regards to the theoretical efforts to derive effective shell-model transition operators starting from realistic potentials, the literature is far less extended, but it is worth mentioning an early review about this topic, which can be found in Ref. [5]. More recently, Suzuki and Okamoto have developed a formalism to derive effective shell-model operators [6], that provides an approach that is consistent with the construction of the corresponding H_{eff} .

In the present work we focus on the derivation of effective shell-model Gamow-Teller (GT) operators to calculate observables related to the β -decay transition for nuclei in different mass regions, aiming to trace back to the roots of the quenching of the free value of the axial coupling constant g_A in nuclear structure calculations.

It should be mentioned that similar studies have been reported in Refs. [7,8]. In Ref. [7], the renormalization of the GT operator, in the form of a one-body operator, has been carried out to study the role of the weak hadronic current in the nuclear medium. The authors of Ref. [8] have instead calculated nuclear matrix elements of the two-neutrino double- β decay ($2\nu\beta\beta$) building an effective two-body operator within the so-called closure approximation.

As a matter of fact, effective GT operators are in general obtained resorting to effective values of g_A , via a quenching factor q , to reproduce experimental GT transitions. The choice of q depends obviously on the nuclear structure model

employed to derive the nuclear wave functions, the dimensions of the considered Hilbert space, and the mass of the nucleus under investigation.

This problem, which affects the calculations of the Gamow-Teller transition strengths and double- β half-lives, has been investigated within different nuclear-structure models, such as the interacting boson model [9–11], the quasi-particle random-phase approximation [12–16], and the shell model [17–26]. In this regard, it is worth mentioning the recent review paper by Suhonen [27], where the quenching is discussed from the points of view of the different methods.

For the sake of clarity, we point out that the quenching of g_A is entangled with both the renormalization of many-body correlations—due to the truncation of the basis used to construct the wave functions—and the corrections due to the subnucleonic structure of the nucleons [28–31], since the free value $g_A^{\text{free}} = 1.2723$ [32] is obtained from the data of the neutron decay under the assumption that the nucleons are point-like particles.

We will show in the following that the perturbative approach to the derivation of effective spin-dependent operators allows to reproduce quantitatively spectroscopic and decay properties without resorting to an empirical quenching either of the axial coupling constant g_A , or of the spin and orbital g factors.

In this connection, it is worth noting that an important contribution to understand the quenching of g_A within a microscopic framework has been given by the studies of Towner and co-workers (see the review paper [33] and references therein), who have extensively investigated the role played by both the many-body correlations induced by the truncation of the Hilbert space and the two-body meson-exchange currents in the renormalization of spin-dependent electromagnetic ($M1$) and weak (GT) operators [34].

Nowadays, there is a renewed interest in the problematics of the renormalization of the GT operator, because of its connection with the calculation of the nuclear matrix elements (NME) of the $0\nu\beta\beta$ decay (see, for example, Ref. [35]). In fact, the half-life of such a process is expressed by

$$[T_{1/2}^{0\nu}]^{-1} = G^{0\nu} |M^{0\nu}|^2 \langle m_\nu \rangle^2, \quad (1)$$

where $G^{0\nu}$ is the so-called phase-space factor, $\langle m_\nu \rangle$ is the effective neutrino mass, and $M^{0\nu}$ is the nuclear matrix element, that relates the wave functions of the parent and grand-daughter nuclei. As a matter of fact, $M^{0\nu}$ can be expressed as the sum of the GT, Fermi (F), and tensor (T) matrix elements, and depends on the axial and vector coupling constants g_A , g_V :

$$M^{0\nu} = M_{\text{GT}}^{0\nu} - \left(\frac{g_V}{g_A}\right)^2 M_F^{0\nu} - M_T^{0\nu}. \quad (2)$$

On these grounds, we focus attention on the renormalization of the GT operator that takes into account the reduced SM model space, without considering the corrections arising from meson-exchange currents [34,36]. Our theoretical framework is the many-body perturbation theory [3,6,37,38], and, starting from a realistic nuclear potential, we derive effective shell-model GT operators and Hamiltonians for nuclei with mass ranging from $A = 48$ to $A = 136$. We also consider in the

derivation of the one-body effective operators the so-called “blocking effect”, to take into account the Pauli exclusion principle in systems with more than one valence nucleon [5].

In Sec. II we will sketch out a few details about the derivation of the effective SM Hamiltonians and operators from a realistic nucleon-nucleon (NN) interaction. The results of the shell-model calculations are then reported in Sec. III. More precisely, we compare calculated and experimental $2\nu\beta\beta$ -decay matrix elements, GT transition-strength distributions for nuclei that are candidates for the detection of the $0\nu\beta\beta$ decay. We extend this analysis to magnetic dipole moments and reduced transition probabilities [$B(M1)$], and, for the sake of completeness, the energy spectra and $B(E2)$ values of the parent and grand-daughter nuclei are also shown. The conclusions of this study are drawn in Sec. IV, together with the outlook of our current project. In the Appendix, tables containing the calculated SP energies of the effective Hamiltonians and the matrix elements of the effective $M1$ and GT operators are reported.

II. OUTLINE OF CALCULATIONS

The cornerstone of a realistic shell-model calculation is the choice of a realistic nuclear potential to start with. We consider for our calculations the high-precision CD-Bonn NN potential [39], whose nonperturbative behavior requires to integrate out its repulsive high-momentum components by way of the so-called $V_{\text{low-k}}$ approach [40,41]. This is based on a unitary transformation that provides a softer nuclear potential defined up to a cutoff Λ , and preserves the physics of the original CD-Bonn interaction.

As in our recent works [38,42–44], the value of the cutoff Λ is chosen equal to 2.6 fm^{-1} , since we have found that the role of missing three-nucleon force (3NF) decreases by enlarging the $V_{\text{low-k}}$ cutoff [43]. In our experience, $\Lambda = 2.6 \text{ fm}^{-1}$ is an upper limit, since with a larger cutoff the order-by-order behavior of the perturbative expansion may be not satisfactory.

This $V_{\text{low-k}}$ is then employed as the two-body interaction term of the Hamiltonian for the system of A nucleons under investigation:

$$H = \sum_{i=1}^A \frac{p_i^2}{2m} + \sum_{i<j=1}^A V_{\text{low-k}}^{ij} = T + V_{\text{low-k}}. \quad (3)$$

This Hamiltonian should be then diagonalized in an infinite Hilbert space to describe the physical observables. Obviously, this task is unfeasible, and in the shell model the infinite number of degrees of freedom is reduced only to those characterizing the physics of a limited number of interacting nucleons, that are constrained in a finite Hilbert space spanned by a few accessible orbitals. To this end, the Hamiltonian H of Eq. (3) is broken up, by way of an auxiliary one-body potential U , into the sum of a one-body term H_0 , whose eigenvectors set up the shell-model basis, and a residual interaction H_1 :

$$\begin{aligned} H &= T + V_{\text{low-k}} \\ &= (T + U) + (V_{\text{low-k}} - U) \\ &= H_0 + H_1. \end{aligned} \quad (4)$$

The following step is to derive an effective shell-model Hamiltonian H_{eff} , that takes into account the degrees of freedom that are not explicitly included in the shell-model framework as the core polarization due to the interaction, within the full Hilbert space, between the valence nucleons and those belonging to the closed core.

We derive H_{eff} by resorting to the many-body perturbation theory an approach that has been developed by Kuo and coworkers through the 1970s [45,46]. More precisely, we use the well-known \hat{Q} box-plus-folded-diagram method [47], where the \hat{Q} box is defined as a function of the unperturbed energy ϵ of the valence particles:

$$\hat{Q}(\epsilon) = PH_1P + PH_1Q \frac{1}{\epsilon - QHQ} QH_1P, \quad (5)$$

where the operator P projects onto the model space and $Q = 1 - P$. In the present calculations the \hat{Q} box is expanded as a collection of one- and two-body irreducible valence-linked Goldstone diagrams up to third order in the perturbative expansion [3,48].

Within this framework the effective Hamiltonian H_{eff} can be written in an operator form as

$$H_{\text{eff}} = \hat{Q} - \hat{Q}' \int \hat{Q} + \hat{Q}' \int \hat{Q} \int \hat{Q} - \hat{Q}' \int \hat{Q} \int \hat{Q} \int \hat{Q} + \dots, \quad (6)$$

where the integral sign represents a generalized folding operation [49], and \hat{Q}' is obtained from \hat{Q} by removing first-order terms [50].

Since the following operatorial identity has been demonstrated [50]:

$$\hat{Q} \int \hat{Q} = -\hat{Q}_1 \hat{Q}, \quad (7)$$

the solution of Eq. (6) may be obtained using the \hat{Q} box derivatives

$$\hat{Q}_m = \frac{1}{m!} \left. \frac{d^m \hat{Q}(\epsilon)}{d\epsilon^m} \right|_{\epsilon=\epsilon_0}, \quad (8)$$

ϵ_0 being the model-space eigenvalue of the unperturbed Hamiltonian H_0 , that we have chosen to be harmonic-oscillator (HO) one.

Consequently, the expression in Eq. (6) may be rewritten as

$$H_{\text{eff}} = \sum_{i=0}^{\infty} F_i, \quad (9)$$

where

$$\begin{aligned} F_0 &= \hat{Q}(\epsilon_0), \\ F_1 &= \hat{Q}_1(\epsilon_0) \hat{Q}(\epsilon_0), \\ F_2 &= [\hat{Q}_2(\epsilon_0) \hat{Q}(\epsilon_0) + \hat{Q}_1(\epsilon_0) \hat{Q}_1(\epsilon_0)] \hat{Q}(\epsilon_0) \\ &\dots \end{aligned} \quad (10)$$

From H_{eff} for one-valence-nucleon systems we obtain the single-particle (SP) energies for our SM calculations, while

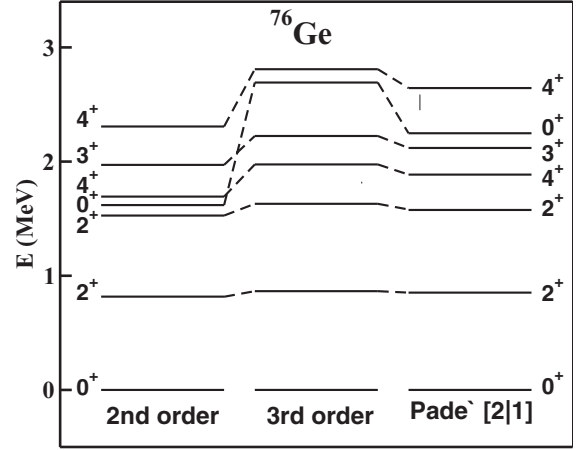


FIG. 1. Calculated spectra of ^{76}Ge obtained from the perturbative expansion of H_{eff} using \hat{Q} -box diagrams up to second-, third-order, and Padé approximant [2|1] (see text for details).

the two-body matrix elements (TBMEs) are obtained from H_{eff} derived for the nuclei with two valence nucleons, by subtracting the theoretical SP energies. The calculated SP energies for ^{40}Ca , ^{56}Ni , and ^{100}Sn cores are reported in the Appendix (see Tables XI–XIII), while the corresponding TBMEs can be found in the Supplemental Material [51].

A detailed description of the perturbative properties of our H_{eff} , derived from the same $V_{\text{low-k}}$ of the present work, can be found in Ref. [52], where the behavior of SP energies and TBME as a function of both the perturbative order and the number of the intermediate states has been reported.

In order to exemplify pictorially the impact of the perturbation expansion on the energy spectra, we report in Fig. 1 the low-energy spectra of ^{76}Ge obtained with H_{eff} s derived from \hat{Q} boxes at second and third order in perturbation theory, and their Padé approximant [2|1] [53]. We employ the Padé approximant in order to obtain a better estimate of the convergence value of the perturbation series [3], as suggested in Ref. [54]. As can be seen, a rather good convergence is obtained, apart from the second-excited $J^\pi = 0^+$ state, the largest discrepancy occurring for the yrare $J^\pi = 4^+$ that is about 20% from second to third order and 6% from third order to Padé approximant [2|1].

As mentioned before, we derive the effective transition operators, namely the matrix elements of the effective spin-dependent $M1$, GT operators, and the effective charges of the electric quadrupole operator, using the formalism presented by Suzuki and Okamoto in Ref. [6].

As a matter of fact, a non-Hermitian effective operator Θ_{eff} can be expressed in terms of the \hat{Q} box, its derivatives, and an infinite sum of operators χ_n , the latter being defined as

$$\chi_0 = (\hat{\Theta}_0 + \text{H.c.}) + \hat{\Theta}_{00}, \quad (11)$$

$$\chi_1 = (\hat{\Theta}_1 \hat{Q} + \text{H.c.}) + (\hat{\Theta}_{01} \hat{Q} + \text{H.c.}), \quad (12)$$

$$\begin{aligned} \chi_2 &= (\hat{\Theta}_1 \hat{Q}_1 \hat{Q} + \text{H.c.}) + (\hat{\Theta}_2 \hat{Q} \hat{Q} + \text{H.c.}) \\ &+ (\hat{\Theta}_{02} \hat{Q} \hat{Q} + \text{H.c.}) + \hat{Q} \hat{\Theta}_{11} \hat{Q}, \dots, \end{aligned} \quad (13)$$

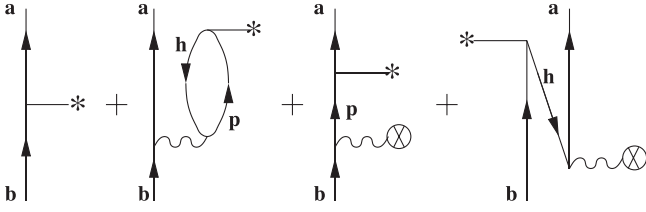


FIG. 2. One-body second-order diagrams included in the perturbative expansion of $\hat{\Theta}$. The asterisk indicates the bare operator Θ , the wavy lines the two-body potential $V_{\text{low-k}}$.

where $\hat{\Theta}_m, \hat{\Theta}_{mm}$ have the following expressions:

$$\hat{\Theta}_m = \frac{1}{m!} \left. \frac{d^m \hat{\Theta}(\epsilon)}{d\epsilon^m} \right|_{\epsilon=\epsilon_0}, \quad (14)$$

$$\hat{\Theta}_{mm} = \frac{1}{m!n!} \left. \frac{d^m}{d\epsilon_1^m} \frac{d^n}{d\epsilon_2^n} \hat{\Theta}(\epsilon_1; \epsilon_2) \right|_{\epsilon_1=\epsilon_0, \epsilon_2=\epsilon_0} \quad (15)$$

with

$$\hat{\Theta}(\epsilon) = P\Theta P + P\Theta Q \frac{1}{\epsilon - QHQ} QH_1P, \quad (16)$$

$$\hat{\Theta}(\epsilon_1; \epsilon_2) = PH_1Q \frac{1}{\epsilon_1 - QHQ} Q\Theta Q \frac{1}{\epsilon_2 - QHQ} QH_1P, \quad (17)$$

Θ being the bare transition operator.

The effective transition operators can be written, in terms of the above quantities, as follows:

$$\Theta_{\text{eff}} = (P + \hat{Q}_1 + \hat{Q}_1\hat{Q}_1 + \hat{Q}_2\hat{Q} + \hat{Q}\hat{Q}_2 + \dots) \times (\chi_0 + \chi_1 + \chi_2 + \dots). \quad (18)$$

Now, inserting the identity $\hat{Q}\hat{Q}^{-1} = \mathbf{1}$ and taking into account Eqs. (9), (10), Eq. (18) may be then recast in the following form:

$$\Theta_{\text{eff}} = (P + \hat{Q}_1 + \hat{Q}_1\hat{Q}_1 + \hat{Q}_2\hat{Q} + \hat{Q}\hat{Q}_2 + \dots) \hat{Q}\hat{Q}^{-1} \times (\chi_0 + \chi_1 + \chi_2 + \dots) = H_{\text{eff}} \hat{Q}^{-1} (\chi_0 + \chi_1 + \chi_2 + \dots). \quad (19)$$

The above form provides a strong link between the derivation of the effective Hamiltonian and all effective operators.

In our calculations for the aforementioned one-body transition operators, we arrest the χ_n series to the χ_2 term. It is worth reminding that in Refs. [38,52] we have included only the leading term χ_0 . The calculation is performed starting from a perturbative expansion of $\hat{\Theta}_0$ and $\hat{\Theta}_{00}$, including diagrams up to the third order in the perturbation theory, consistent with the perturbative expansion of the \hat{Q} box. We have found that the χ_2 contribution is at most 1% of the final results. Since χ_3 depends on the first, second, and third derivatives of $\hat{\Theta}_0$ and $\hat{\Theta}_{00}$, and on the first and second derivatives of the \hat{Q} box [see Eq. (13)], our estimation of these quantities leads to evaluate χ_3 being at least one order of magnitude smaller than χ_2 .

For the sake of clarity, in Fig. 2 we report all the one-body Θ_0 diagrams up to the second order, the bare operator Θ being represented with an asterisk. The first-order ($V_{\text{low-k}} - U$) insertion, represented by a circle with a cross inside, arises

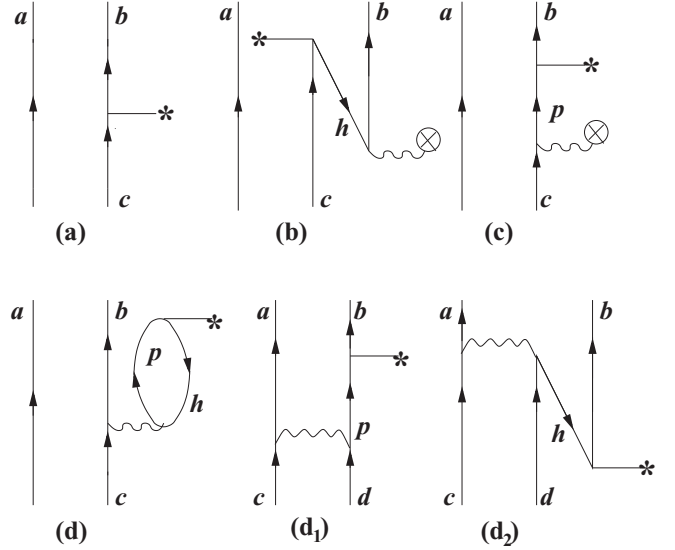


FIG. 3. Two-body second-order diagrams that should appear in the perturbative expansion of χ_0 . As in Fig. 2, the asterisk indicates the bare operator Θ , the wavy lines the two-body potential $V_{\text{low-k}}$.

because of the presence of the U term in the interaction Hamiltonian H_1 (see, for example, Ref. [3] for details).

In Ref. [52] we have carried out a study of the perturbative properties of the GT operator for the calculation of the NME ($M_{\text{GT}}^{2\nu}$) of the ^{130}Te , $^{136}\text{Xe}2\nu\beta\beta$ decay. We have found that the results for the ^{130}Te decay vary by about 10% from second to third order in perturbation theory, and that for ^{136}Xe by about 5%.

As it regards the magnetic-dipole operator, we find a similar perturbative behavior. As a matter of fact, the calculated magnetic dipole moments of the yrast $J^\pi = 2^+$ states in ^{130}Te and ^{136}Xe , obtained with an effective operator derived at second order in perturbation theory, are 0.65 and 1.19 μ_N , respectively, to be compared with 0.71 and 1.15 μ_N at third order (see also Tables VII and IX.) The variation from second to third order is about 8% for ^{130}Te , and 3% for ^{136}Xe .

The authors of Ref. [7] have carried out a perturbative expansion of the $\hat{\Theta}$ operator for GT transitions in terms of similar diagrams, calculated up to third order in perturbation theory and employing G -matrix energy-dependent interaction vertices. They have added to them the corresponding folded diagrams according to the prescription of Ref. [33], but have neglected all diagrams with $(G - U)$ -insertion vertices, which—it is worth pointing out—at second order only are equal to zero for spin-dependent operators.

They have reported a selection of the matrix elements of their effective GT^+ operator, that we compare with our results in Tables XVII–XIX. As can be observed, both calculations provide consistent results, even if some matrix elements differ up to 25%.

The topology of the diagrams reported in Fig. 2 deals, obviously, with single-valence nucleon systems, and many-body diagrams should be included starting from nuclei with two valence nucleons on; in Fig. 3 we report all two-valence-nucleon diagrams for one-body operators, up to second order

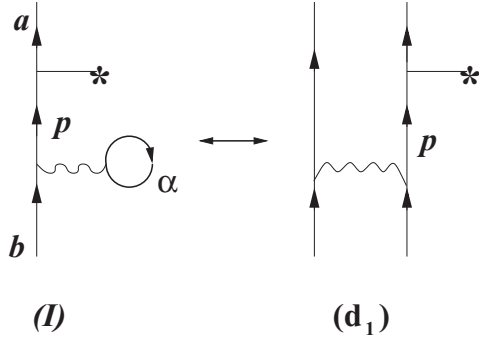


FIG. 4. Density-dependent one-body second-order diagram (I) that is obtained from diagram (d_1) of Fig. 2 by summing over one incoming and outgoing particles of the two-body diagram (see text for details).

of the $\hat{\Theta}$ perturbative expansion. For the sake of simplicity, for each topology we draw only one of the diagrams which correspond to the exchange of the external pairs of lines.

Diagrams (a)–(d) are the same as in Fig. 2 but with a spectator line a , while connected diagrams (d_1) and (d_2) correct Pauli-principle violation introduced by diagram (d) when the particles c and p own the same quantum numbers.

Since it is straightforward to perform shell-model calculations using one-body transition operators, we derive a density-dependent one-body operator from the two-body ones by summing and averaging over one incoming and outgoing particles of the connected diagrams (d_1) and (d_2) of Fig. 3. This allows to take into account the filling of the model-space orbitals when dealing with more than one valence nucleon.

For example, we report in Fig. 4 the second-order density-dependent one-body diagram (I), obtained from the contribution (d_1) of Fig. 3, and whose explicit expression is

$$(I) = \sum_{\alpha} \sum_{p'} \frac{(2J+1)}{(2j_b+1)} \frac{\langle a || \Theta || p \rangle \langle p \alpha, J | V_{\text{low-}k} | b \alpha, J \rangle}{(\epsilon_b - \epsilon_p)} \rho(\alpha), \quad (20)$$

where α and p indices run over the orbitals in, and above the model space, respectively, the matrix elements of the $V_{\text{low-}k}$ are coupled to the total angular momentum J , ϵ_i stands for the unperturbed energy of the orbital i , and $\rho(\alpha)$ is the occupation probability of the orbital α .

In this work all the results of the shell-model calculations, that are shown in Sec. III, have been obtained employing SP energies, TBMEs, and effective one-body operators derived by way of the above mentioned theoretical approach, including consistently all contributions up to third order in the perturbative expansion, without resorting to any empirically fitted parameter.

In Sec. III, the calculated running sums of the GT strengths [$\Sigma B(p, n)$], obtained with both bare and effective GT operators, are reported as a function of the excitation energy, and compared with the available data extracted from experiment. The GT strength is defined as

$$B(p, n) = \frac{|\langle \Phi_f || \sum_j \vec{\sigma}_j \tau_j^- || \Phi_i \rangle|^2}{2J_i + 1}, \quad (21)$$

where indices i, f refer to the parent and grand-daughter nuclei, respectively, and the sum is over all interacting nucleons.

The single- β decay GT strengths, defined by Eq. (21), can be accessed experimentally through intermediate energy charge-exchange reactions, since the β -decay process is forbidden for the nuclei under our investigation. The GT strength can be extracted from the GT component of the cross section at zero degree, following the standard approach in the distorted-wave Born approximation (DWBA) [55,56]:

$$\frac{d\sigma^{\text{GT}}(0^\circ)}{d\Omega} = \left(\frac{\mu}{\pi \hbar^2} \right)^2 \frac{k_f}{k_i} N_D^{\sigma\tau} |J_{\sigma\tau}|^2 B(p, n), \quad (22)$$

where $N_D^{\sigma\tau}$ is the distortion factor, $|J_{\sigma\tau}|$ is the volume integral of the effective NN interaction, k_i and k_f are the initial and final momenta, respectively, and μ is the reduced mass.

As regards the calculation of the NME of the $2\nu\beta\beta$ decay, it can be obtained via the following expression:

$$M_{\text{GT}}^{2\nu} = \sum_n \frac{\langle 0_f^+ || \vec{\sigma} \tau^- || 1_n^+ \rangle \langle 1_n^+ || \vec{\sigma} \tau^- || 0_i^+ \rangle}{E_n + E_0}, \quad (23)$$

where E_n is the excitation energy of the $J^\pi = 1_n^+$ intermediate state, $E_0 = \frac{1}{2} Q_{\beta\beta}(0^+) + \Delta M$, $Q_{\beta\beta}(0^+)$ and ΔM being the Q value of the $\beta\beta$ decay and the mass difference between the daughter and parent nuclei, respectively. In the above equation the index n runs over all possible intermediate states of the daughter nucleus. The NMEs have been calculated using the ANTOINE shell-model code, using the Lanczos strength-function method as in Ref. [57], and including as many as intermediate states to obtain at least a four-digit accuracy (see also Figs. 5, 11 in Ref. [38]). The theoretical values are then compared with the experimental counterparts, that are extracted from the observed half life $T_{1/2}^{2\nu}$,

$$[T_{1/2}^{2\nu}]^{-1} = G^{2\nu} |M_{\text{GT}}^{2\nu}|^2. \quad (24)$$

The calculation of $M_{\text{GT}}^{2\nu}$ may be also performed without calculating explicitly the intermediate $J^\pi = 1_n^+$ states of the daughter nucleus, namely resorting to the so-called closure approximation [58]. The price to be paid is that the transition operator is no longer a one-body operator but a two-body one. It is worth pointing out that this approximation is largely employed to calculate the $0\nu\beta\beta$ NME ($M^{0\nu}$), since the high momentum of the neutrino—which appears explicitly in the definition of $M^{0\nu}$ —is about 100 MeV that is one order of magnitude greater than the average $J^\pi = 1_n^+$ excitation energy. As a matter of fact, it has been estimated that this approximation is valid within 10% of the exact result [59]. Actually, the same approximation has turned out to be very unsatisfactory for the calculation of $M_{\text{GT}}^{2\nu}$, because the energies of the neutrinos which are emitted in the $2\nu\beta\beta$ process are much smaller. For instance, in Ref. [8] the authors obtain a result for ^{76}Ge $M_{\text{GT}}^{2\nu}$ that is about two times larger than the one calculated with the Lanczos strength-function method by employing the same SM wave functions [25,60], and about 5 times larger than the experimental value [61].

III. RESULTS

In this section we present the results of our SM calculations. We compare the calculated low-energy spectra of ^{48}Ca ,

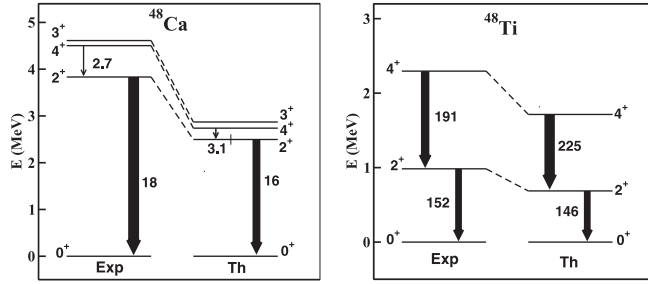


FIG. 5. Experimental and calculated spectra of ^{48}Ca and ^{48}Ti . $B(E2)$ strengths (in $e^2\text{fm}^4$) are also reported (see text for details).

^{48}Ti , ^{76}Ge , ^{76}Se , ^{82}Se , ^{82}Kr , ^{130}Te , ^{130}Xe , ^{136}Xe , and ^{136}Ba , and their electromagnetic properties with the available experimental counterparts. As mentioned in the Introduction, special attention will be focused on the magnetic dipole properties, since both $M1$ and GT operators are spin dependent.

We show also the results of the GT^- strength distributions and the calculated NMEs of the $2\nu\beta\beta$ decays for ^{48}Ca , ^{76}Ge , ^{82}Se , ^{130}Te , and ^{136}Xe , and compare them with the available data. All the calculations have been performed employing theoretical SP energies, TBMEs, and effective transition operators. In particular, for the $M1$ and GT properties we report the calculated values obtained by using the bare (I) and effective (II) operators, as well as those including the blocking effect—and labeled as (III)—by way of a density-dependent effective operator as mentioned in Sec. II. The latter give us the opportunity to investigate the role of many-body correlations on the spin- and spin-isospin-dependent one-body operators in nuclei with more than one valence nucleon.

A. ^{48}Ca

The shell-model calculation for ^{48}Ca and ^{48}Ti are performed within the full fp shell, namely the proton and neutron $0f_{7/2}$, $0f_{5/2}$, $1p_{3/2}$, and $1p_{1/2}$ orbitals. In Fig. 5, we show the experimental [62,63] and calculated low-energy spectra of ^{48}Ca and ^{48}Ti . Next to the arrows, that are proportional to the $B(E2)$ strengths, we report the explicit experimental [62,63] and calculated $B(E2)$ s in $e^2\text{fm}^4$.

As can be seen, we do not reproduce the observed shell closure of the neutron $0f_{7/2}$ orbital in ^{48}Ca and the agreement between the experimental and calculated spectra is only qualitative, while experimental $B(E2)$ s are satisfactorily reproduced by the theory.

In Table I the low-energy experimental and calculated observable related to the $M1$ operator are reported. The calculated values reported in columns I, II, III are obtained with the bare magnetic-dipole operator, the effective one without blocking effect, and the one including the blocking effect, respectively.

From an inspection of Table I, it can be seen that the calculated magnetic-dipole transition rates $B(M1)$ s compare well with the observed value for ^{48}Ca . In particular, from Table XIV, the values obtained employing the effective shell-model operators (II,III) are quenched with respect to that calculated with the bare operator (I), and in a better agreement

TABLE I. Experimental and calculated $B(M1)$ strengths (in μ_N^2) and magnetic dipole moments (in μ_N) of ^{48}Ca and ^{48}Ti . We report those for the observed states in Fig. 5 (see text for details).

Nucleus	$J_i \rightarrow J_f$	$B(M1)_{\text{exp}}$	I	II	III
^{48}Ca	$3^+ \rightarrow 2^+$	0.023 ± 0.004 [64]	0.051	0.046	0.046
	J	μ_{exp}	I	II	III
^{48}Ti	2^+	$+0.78 \pm 0.04$ [62]	+0.37	+0.54	+0.54
		$+0.9 \pm 0.4$ [62]			
	4^+	$+2.2 \pm 0.5$ [62]	+1.2	+1.5	+1.5

with experiment. The blocking effect is very tiny because the number of valence nucleons is rather small compared with the full capacity of the fp shell.

Regarding the magnetic moments, data are available for ^{48}Ti , and they are underestimated by the theory. However, the contribution due to the effective operators points in the right direction, leading to a better agreement with experiment.

In Table II we report the observed and calculated values of the NMEs for the $2\nu\beta\beta$ decay of ^{48}Ca into ^{48}Ti . The NME obtained with the bare operator (I) slightly underestimates the experimental one, and it is 20% larger than those obtained with the effective operators (II) and (III). This corresponds to a quenching factor $q = 0.9$, that is roughly the average value of the reduction factor that can be extracted from Table XVII, comparing the single-particle elements of the bare GT operator with the effective ones. In this context, it should be mentioned that our $2\nu\beta\beta$ NME calculated with the bare operator is very different from those obtained by way of SM calculations employing phenomenological H_{eff} [20,21], which reproduce correctly the observed shell closure of $0f_{7/2}$ orbital in ^{48}Ca .

It is worth noting that, as for the $M1$ properties, the blocking effect plays a negligible role also in the calculation of the $2\nu\beta\beta$ NME.

In Fig. 6, the calculated $\Sigma B(p, n)$ for ^{48}Ca are shown as a function of the excitation energy, and compared with the data reported with a red line [65]. The results obtained with the bare operator (I) are drawn with a blue line, while those obtained employing the effective GT operators without and with the blocking effect are plotted using continuous and dashed black lines, respectively.

It can be seen that the distribution obtained using the bare operator (I) overestimates the observed one, and it is very close to those provided by both the effective GT operators (II,III), the blocking effect being almost negligible. Finally, we report about the theoretical total GT^- strengths that are

TABLE II. Experimental [61] and calculated NME of the $2\nu\beta\beta$ decay (in MeV^{-1}) for ^{48}Ca . The same notation of Table I is used (see text for details).

Decay	NME_{exp}	I	II	III
$^{48}\text{Ca} \rightarrow ^{48}\text{Ti}$	0.038 ± 0.003	0.030	0.026	0.026

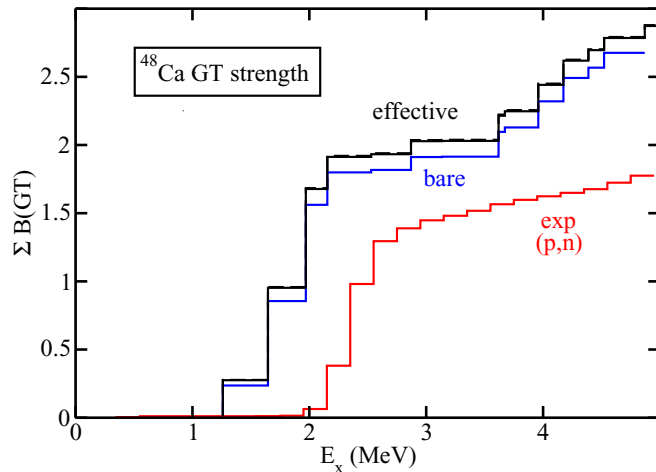


FIG. 6. Running sums of the ^{48}Ca $B(p, n)$ strengths as a function of the excitation energy E_x up to 5 MeV (see text for details).

24.0, 23.1, and 23.0 with the bare operator (I), and the effective ones (II) and (III), respectively.

B. ^{76}Ge

The shell-model calculations for ^{76}Ge and ^{76}Se are performed within the model space spanned by the four proton and neutron orbitals $0f_{5/2}$, $1p_{3/2}$, $1p_{1/2}$, and $0g_{9/2}$, considering ^{56}Ni as a closed core. The experimental [62,63] and calculated low-energy spectra of ^{76}Ge and ^{76}Se are reported in Fig. 7, together with the experimental [62,63] and calculated $B(E2)$ strengths (in $e^2\text{fm}^4$), as in Fig. 5.

The agreement between the experimental and calculated spectra and $B(E2)$ s is far more satisfactory than that obtained for $A = 48$.

In Table III we report the experimental and calculated $B(M1)$ strengths as well as magnetic dipole moments of ^{76}Ge and ^{76}Se .

It can be observed that, with respect to the calculations for ^{48}Ca and ^{48}Ti , now the contribution arising from an effective transition operator—whose matrix elements are reported in Table XV—is more relevant, and significantly improves the comparison with data. This traces back to the fact that, as it is well known [33], spin- and spin-isospin-dependent operators need larger renormalizations when orbitals belonging to the

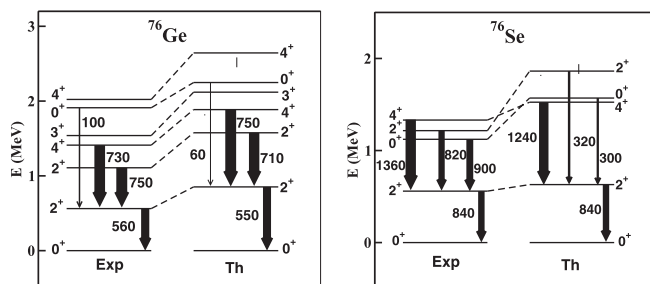


FIG. 7. Same as in Fig. 5, but for ^{76}Ge and ^{76}Se (see text for details).

TABLE III. Same as in Table I, but for ^{76}Ge and ^{76}Se (see text for details).

Nucleus	$J_i \rightarrow J_f$	$B(M1)_{\text{exp}}$	I	II	III
^{76}Ge	$2_2^+ \rightarrow 2_1^+$	$0.003^{+0.002}_{-0.003}$ [66]	0.006	0.004	0.005
	$4_2^+ \rightarrow 3_1^+$	0.02 ± 0.01 [66]	0.062	0.027	0.025
		0.002 ± 0.001 [66]			
	$4_2^+ \rightarrow 4_1^+$	$0.03^{+0.02}_{-0.03}$ [66]	0.07	0.03	0.03
		0.04 ± 0.02 [66]			
Nucleus	J	μ_{exp}	I	II	III
^{76}Ge	2_1^+	$+0.64 \pm 0.02$ [67]	+0.53	+0.83	+0.84
	2_2^+	$+0.78 \pm 0.10$ [67]	+0.93	+1.10	+1.09
	4_1^+	$+0.96 \pm 0.68$ [67]	+0.58	+1.33	+1.36
^{76}Se	2_1^+	0.81 ± 0.05 [68]	+0.37	+0.60	+0.58
	2_2^+	0.70 ± 0.12 [68]	+0.64	+0.82	+0.79
	4_1^+	2.6 ± 0.4 [68]	+0.3	+0.9	+0.9

model space lack their spin-orbit counterpart. As a matter of fact, this regards single-body matrix elements of the effective $M1$ —and GT operators—involving the $0f_{5/2}$ and $0g_{9/2}$ orbitals. We observe that also for ^{76}Ge and ^{76}Se , the blocking effect on the $M1$ operator seems rather unimportant.

As regards the comparison with experiment, both calculated $B(M1)$ s and dipole moments agree with data, especially those obtained with the effective operators (II) and (III). It is worth pointing out that, using the effective operators, the quenching of the nondiagonal one-body matrix elements in Table XV is responsible for the reduction of the calculated $B(M1)$ s with respect to those obtained with the bare operator. On the other side, the enhancement of the proton diagonal matrix element $\langle 0f_{5/2} || M1 || 0f_{5/2} \rangle$ (see Table XV) leads to an increase of the magnetic dipole moments of the yrast states.

As can be seen in Table XVIII, the renormalization effect of the GT operator is much stronger than that observed for the $M1$ operator. This is reflected in our shell-model results for the NMEs of the $2\nu\beta\beta$ decay of ^{76}Ge into ^{76}Se , that are compared with the experimental value [61] in Table IV.

From the inspection of Table IV, it can be observed that using the bare GT operator (I) the calculated NME overestimates the datum by almost a factor of 3, and this gap is recovered employing the effective operator (II) which introduces an average quenching factor $q \simeq 0.6$. As a matter of fact, this renormalization leads to a theoretical result that is very close to the experimental one. Moreover, it can be observed that a tiny blocking effect pushes the calculated value (III) within the experimental error.

TABLE IV. Same as in Table II, but for the $2\nu\beta\beta$ decay of ^{76}Ge (see text for details).

Decay	NME_{Exp}	I	II	III
$^{76}\text{Ge} \rightarrow ^{76}\text{Se}$	0.113 ± 0.006	0.304	0.095	0.104

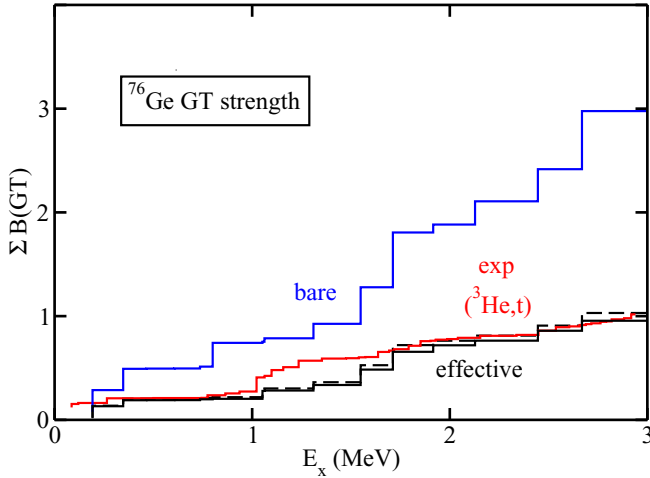


FIG. 8. Running sums of the ^{76}Ge $B(p, n)$ strengths as a function of the excitation energy E_x up to 3 MeV (see text for details).

The role played by the effective operator is also evident when we compare the calculated and experimental [69] $\Sigma B(p, n)$ for ^{76}Ge as a function of the excitation energy. This is done in Fig. 8, where the running sums of the GT strengths are reported up to a 3 MeV excitation energy. Note that the same notation as in Fig. 6 is used here.

This figure, as Table IV, evidences how crucial it is to take into account the renormalization of the GT operator to obtain a good agreement between theory and experiment. It is worth adding that the contribution of the blocking effect is almost irrelevant.

For the sake of completeness, we have calculated the theoretical total GT^- strengths, and obtained the values 18.2, 6.9, and 7.2 with the bare operator (I), and the effective ones (II) and (III), respectively.

C. ^{82}Se

As for ^{76}Ge and ^{76}Se , the shell model calculation for ^{82}Se and ^{82}Kr has been carried out using, as model space, the four proton and neutron orbitals $0f_{5/2}$, $1p_{3/2}$, $1p_{1/2}$, and $0g_{9/2}$ placed outside ^{56}Ni . In Fig. 9 the calculated low-energy spectra and $B(E2)$ s are compared with experiment [62,63].

The agreement between theory and experiment can be considered satisfactory, the largest discrepancy, in both nuclei,

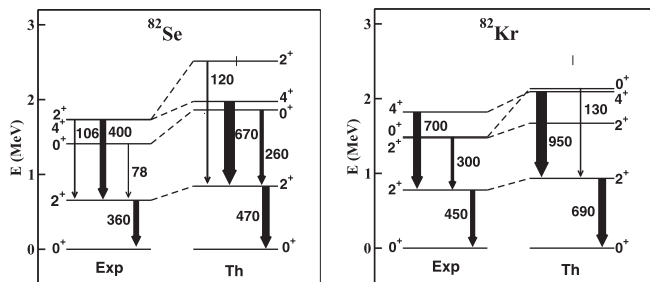


FIG. 9. Same as in Fig. 5, but for ^{82}Se and ^{82}Kr (see text for details).

TABLE V. Experimental and calculated magnetic dipole moments (in nm) of ^{82}Se and ^{82}Kr . We report those for the observed states in Fig. 9.

Nucleus	J	μ_{exp}	I	II	III
^{82}Se	2_1^+	$+0.99 \pm 0.06$ [62]	+0.72	+1.03	+1.05
	4_1^+	2.3 ± 1.5 [62]	+1.17	+1.88	+1.93
^{82}Kr	2_1^+	$+0.80 \pm 0.04$ [62]	+0.50	+0.83	+0.83
	4_1^+	$+1.2 \pm 0.8$ [62]	+0.5	+1.3	+1.3

occurring for the $B(E2; 0_2^+ \rightarrow 2_1^+)$ s, whose calculated values are about a factor 3 smaller than the observed ones.

Regarding the observables linked to the $M1$ operator, the only available data for the low-lying states reported in Fig. 9 are the magnetic dipole moments shown in Table V.

Since the model space is the same as for $A = 76$ nuclei, the matrix elements of the effective $M1$ operator (II) are those reported in Table XV. The action of the effective operators, as can be observed from the inspection of Table V, is to improve the comparison with the data of the shell-model results, with respect to those obtained with the bare operator (I). This result evidences the role of the renormalization of the bare operator to take into account the degrees of freedom that have been left out by constraining the nuclear wave function to the valence nucleons interacting in the truncated model space.

As for the $2\nu\beta\beta$ decay of ^{76}Ge , the quenching of the matrix elements of the GT operator, shown in Table XVIII, is crucial to improve our calculation of the NME of the decay of ^{82}Se into ^{82}Kr . In fact, the NME calculated with the bare operator overestimates the experimental value [61] by a factor 4, as can be inferred from Table VI, while calculations performed with the effective operators (II,III) provide far better results.

The quenching of the effective GT operator is a feature that is crucial also in providing a calculated $\Sigma B(p, n)$ curve for ^{82}Se , as a function of the excitation energy, that almost overlaps with the experimental one [70], as can be seen in Fig. 10 where the running sums of the ^{82}Se GT strengths up to a 3 MeV excitation energy are reported.

As for the calculations of ^{48}Ca , ^{76}Ge $\Sigma B(p, n)$, we observe a negligible role of the blocking effect.

We conclude this section reporting the calculated total GT^- strengths that are 21.6, 8.5, and 8.9 with the bare operator (I), and the effective ones (II) and (III), respectively.

D. ^{130}Te

The shell-model calculations for ^{130}Te and ^{130}Xe are performed within the model space spanned by the five proton and

TABLE VI. Same as in Table II, but for the $2\nu\beta\beta$ decay of ^{82}Se (see text for details).

Decay	NME_{Expt}	I	II	III
$^{82}\text{Se} \rightarrow ^{82}\text{Kr}$	0.083 ± 0.004	0.347	0.111	0.109

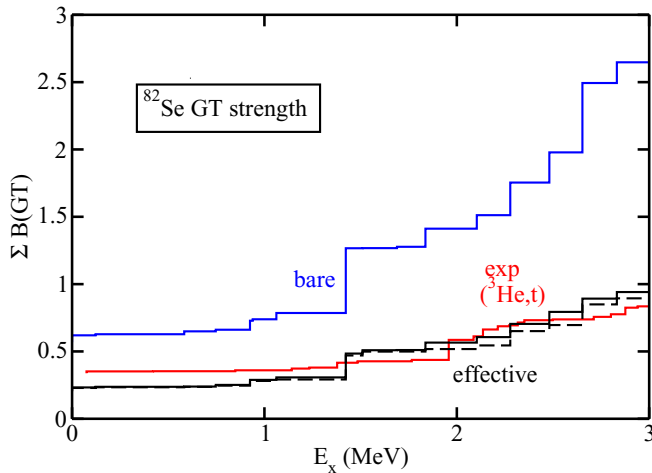


FIG. 10. Running sums of the ^{82}Se $B(p, n)$ strengths as a function of the excitation energy E_x up to 3 MeV (see text for details).

neutron orbitals $0g_{7/2}$, $1d_{5/2}$, $1d_{3/2}$, $2s_{1/2}$, and $0h_{11/2}$, considering ^{100}Sn as a closed core. For the sake of completeness, the experimental [62,63] and calculated low-energy spectra and $B(E2)$ s, already reported in Ref. [38], are also presented in this work in Fig. 11.

From an inspection of Fig. 11, we observe that the comparison between the calculated and experimental low-energy spectra is very good for ^{130}Te , while it is less satisfactory for ^{130}Xe . As regards the calculated $B(E2)$ s, they compare well with the observed values for both nuclei, providing good expectations about the reliability of the SM wave functions.

In Table VII the calculated $B(M1; 2_3^+ \rightarrow 2_1^+)$ of ^{130}Te is reported and compared with the two experimental values of Ref. [71]. In the same table the calculated and observed magnetic dipole moments of ^{130}Te and ^{130}Xe can be found.

As can be seen, similar to the results of the calculations for ^{76}Ge and ^{82}Se , the role of the effective $M1$ operator is relevant. As a matter of fact, the smaller $B(M1)$ values, compared with the one calculated with the bare operator, are a consequence of the general quenching of the nondiagonal matrix elements reported in Table XVI. On the other side, the enhancement of the proton $0g_{7/2}$ diagonal matrix element is responsible for the larger dipole moments, when they are calculated employing the effective operators (II) and (III). Actually, because of the large experimental errors, it is not clear if the effective oper-

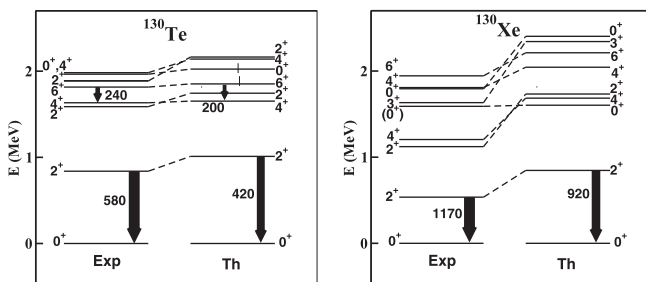


FIG. 11. Same as in Fig. 5, but for ^{130}Te and ^{130}Xe (see text for details).

TABLE VII. Same as in Table I, but for ^{130}Te and ^{130}Xe (see text for details). We report those for the observed states in Fig. 11.

Nucleus	$J_i \rightarrow J_f$	$B(M1)_{\text{exp}}$	I	II	III
^{130}Te	$2_3^+ \rightarrow 2_1^+$	$0.037^{+0.03}_{-0.04}$ [71]	0.057	0.085	0.077
		$0.097^{+0.08}_{-0.11}$ [71]			
Nucleus	J	μ_{exp}	I	II	III
^{130}Te	2_1^+	0.58 ± 0.10 [62]	+0.52	+0.71	+0.71
^{130}Xe	2_1^+	0.57 ± 0.14 [62]	+0.50	+0.67	+0.66

ators are able to provide a better agreement with experiment for the dipole moments with respect to the bare operator. As it regards the $B(M1; 2_3^+ \rightarrow 2_1^+)$, it turns out that our calculated values are closer to the smallest of the two values reported in Ref. [71]. Finally, it is worth noting that there is no sizable role of the blocking effect.

The calculated and experimental values of the NME for the ^{130}Te $2\nu\beta\beta$ decay [61] are reported in Table VIII.

As shown in our previous study [38], the quenching of the bare operator (I) provided by the effective ones (II,III) (see Table XVII) plays a fundamental role to obtain a reasonable comparison with the experimental NME. As a matter of fact, our shell model calculation gives a $2\nu\beta\beta$ NME that is almost 4 times bigger than the experimental one, starting from GT operator (I). On the other hand, the effective operators, derived via many-body perturbation theory, take into account the reduction of the full Hilbert space to configurations constrained by the valence nucleons interacting in the model space and provide NMEs that are almost within experimental error bars.

These considerations hold, obviously, also for the calculation of the ^{130}Te $\Sigma B(p, n)$, whose results are reported in Fig. 12 and compared with available data [72] up to 3 MeV excitation energy.

As for the ^{76}Ge and ^{82}Se running sums, the curves obtained with the effective operators (II,III) lie much closer to the experimental one than that calculated employing the bare operator (I), and almost overlap each other.

The total GT^- strengths, obtained with effective operators (I–III), are 46.4, 18.3, and 18.6, respectively.

E. ^{136}Xe

The shell-model calculations for ^{136}Xe and ^{136}Ba are carried out using the same model space, effective Hamiltonian, and transition operators as for ^{130}Te and ^{130}Xe , and details

TABLE VIII. Same as in Table II, but for the $2\nu\beta\beta$ decay (in MeV^{-1}) of ^{130}Te (see text for details).

Decay	NME_{exp}	I	II	III
$^{130}\text{Te} \rightarrow ^{130}\text{Xe}$	0.031 ± 0.004	0.131	0.057	0.061

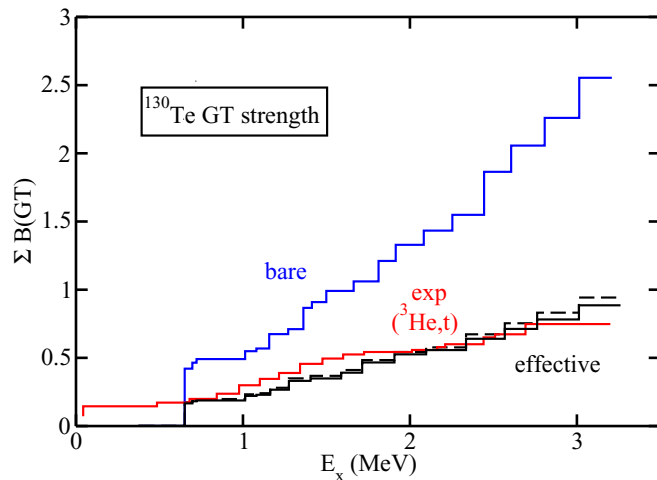


FIG. 12. Running sums of the ^{130}Te $B(p, n)$ strengths as a function of the excitation energy E_x up to 3 MeV (see text for details).

about SP energies, TBMEs, effective charges, and effective GT matrix elements can be found in Ref. [38].

We present, as in our previous study, the experimental [62,63] and calculated low-energy spectra and $B(E2)$ s which we have reported in Fig. 13.

The comparison between theory and experiment, as it regards the low-lying excited states and the $B(E2)$ transition rates, is excellent for both nuclei, showing once more the reliability of the realistic shell model.

In Table IX we report the calculated and experimental $B(M1)$ s of ^{136}Ba , involving some of the excited states reported in Fig. 13, together with the $J = 2_1^+$ magnetic dipole moment. We compare also theory and experiment for the $J = 2_1^+, 4_1^+$ magnetic dipole moments of ^{136}Xe .

As a matter of fact, we observe the same tendency we have found in the previous calculations, that is the quenching of $B(M1)$ values obtained with effective operators (II,III), and the enhancement of the dipole moments when the same operators are employed. This is grounded on the same observations we have made in Sec. III D, and supported by the inspection of the list of the matrix elements in Table XVI.

Actually, both features lead to an improvement in the description of the data, and support again the crucial role of the renormalization of transition operators by way of the many-body perturbation theory.

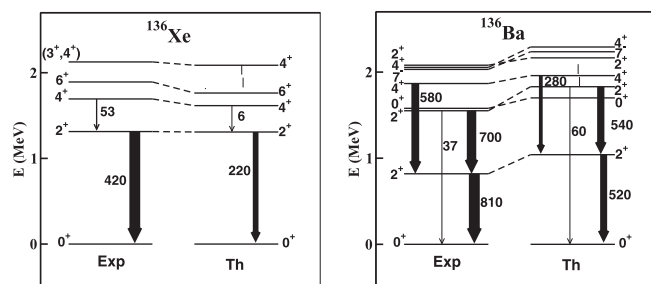


FIG. 13. Same as in Fig. 5, but for ^{136}Xe and ^{136}Ba (see text for details).

TABLE IX. Same as in Table I, but for ^{136}Xe and ^{136}Ba (see text for details). We report those for the observed states in Fig. 13.

Nucleus	$J_i \rightarrow J_f$	$B(M1)_{\text{exp}}$	I	II	III
^{136}Ba	$2_2^+ \rightarrow 2_1^+$	0.02 ± 0.1 [73]	0.07	0.06	0.06
	$2_3^+ \rightarrow 2_1^+$	0.002 ± 0.002 [73]	0.006	0.002	0.001
	$4_2^+ \rightarrow 4_1^+$	$0.06_{-0.05}^{+0.08}$ [73]	0.15	0.10	0.09
Nucleus	J	μ_{exp}	I	II	III
^{136}Xe	2_1^+	1.53 ± 0.09 [62]	+1.05	+1.15	+1.14
	4_1^+	3.2 ± 0.6 [62]	+2.02	+2.24	+2.22
^{136}Ba	2_1^+	0.69 ± 0.10 [62]	+0.48	+0.60	+0.59

This consideration is even more valid when we consider the calculation of the NME for the ^{136}Xe $2\nu\beta\beta$ decay, whose results are reported in Table X and compared with the datum [61].

We see that the (II,III) NMEs are more than a factor of 3 smaller than the value obtained with the bare operator (I), and closer to the experimental value. The same feature comes out in Fig. 14, where we report the calculated and experimental [74] $\Sigma B(p, n)$ of ^{136}Xe up to 4.5 MeV excitation energy.

Also for the ^{136}Xe running sums, the many-body renormalization of the GT operator is crucial to reproduce the experimental curve with a negligible contribution of the blocking effect.

The total GT^- strengths, obtained with bare and effective operators (I–III), are 51.9, 20.7, and 21.0, respectively.

IV. CONCLUSIONS AND OUTLOOK

In this paper we have studied the role of effective operators to calculate, within the realistic shell model, observables that are related to spin- and spin-isospin-dependent transitions. Our main focus has been on GT transitions for nuclei that are candidates for the detection of the $0\nu\beta\beta$ decay, and we have calculated, for several nuclei and over a wide mass range, $2\nu\beta\beta$ -decay NMEs and the running sums of the $B(p, n)$ strengths to compare them with the available data. Since the magnetic-dipole $M1$ operator incorporates an isovector-spin term with the same structure of the GT operator, we have extended this analysis to the calculation of $B(M1)$ s and magnetic dipole moments to strengthen our investigation.

As a matter of fact, our aim has been to demonstrate that the present status of the many-body perturbation theory allows to derive consistently effective Hamiltonians and transition operators that are able to reproduce quantitatively the observed spectroscopic and decay properties, without resorting

TABLE X. Same as in Table II, but for the $2\nu\beta\beta$ decay (in MeV^{-1}) of ^{136}Xe (see text for details).

Decay	NME_{exp}	I	II	III
$^{136}\text{Xe} \rightarrow ^{136}\text{Ba}$	0.0181 ± 0.0007	0.0910	0.0332	0.0341

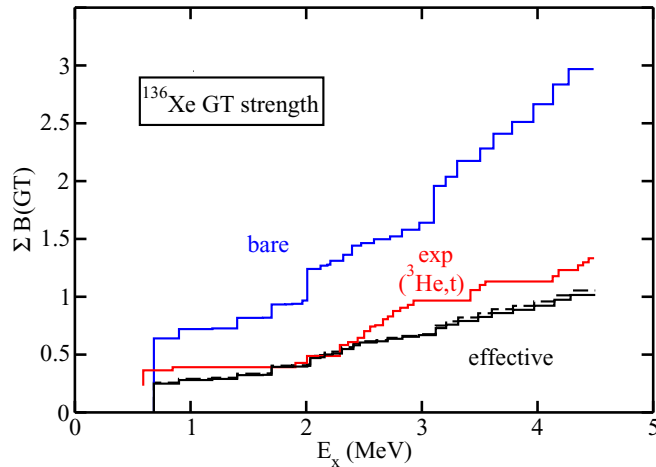


FIG. 14. Running sums of the ^{136}Xe $B(p, n)$ strengths as a function of the excitation energy E_x up to 4.5 MeV (see text for details).

to an empirical quenching of the axial coupling constant g_A , or to empirically fitted spin and orbital g factors g_s, g_l .

The quenching factors corresponding to the matrix elements of the effective $M1$ and GT operators are reported in Tables XIV–XVI and Tables XVII–XIX, respectively. It is worth noting that the calculated quenching effect on the $M1$ operator is overall smaller than for GT transitions, which points to the fact that the two operators are differently affected by the renormalization procedure. This result highlights that for the renormalization of the $M1$ operator a non-negligible role is played by its isoscalar and isovector orbital components. As a matter of fact, from the inspection of these tables, the quenching of proton-proton $M1$ matrix elements is overall largely different from the GT one, the latter being much closer to that obtained for neutron-neutron $M1$ matrix elements (which own the spin component only).

In order to show and stress pictorially the main outcome of our study about the relevance played by effective transition operators, in Fig. 15 we report a correlation plot between our calculated $2\nu\beta\beta$ decay NMEs and the corresponding experimental values. The quantities in Fig. 15 are already reported in Tables II, IV, VI, VIII, X.

The red symbols correspond to the results obtained employing the bare operators (I), while the black ones indicate the results obtained with the effective operators (III).

As can be seen, the red points are all spread on the lower side of the figure, except the one corresponding to ^{48}Ca , and lie far away from the identity, that is represented by a dashed line. This feature characterizes the nuclei that are described by way of a model space where some of its orbitals lack their spin-orbit counterparts, leading to an overestimation of the calculated NME with respect to the experimental value.

The black points, that correspond to the effective GT operators, on the other hand regroup themselves close to the identity, as a reliable calculation should do.

It is worth reminding the reader that our results may be traced back to earlier investigations carried out by Towner and collaborators since the 1980s (see, for instance, [33,34,75,76]), where the role of microscopically derived

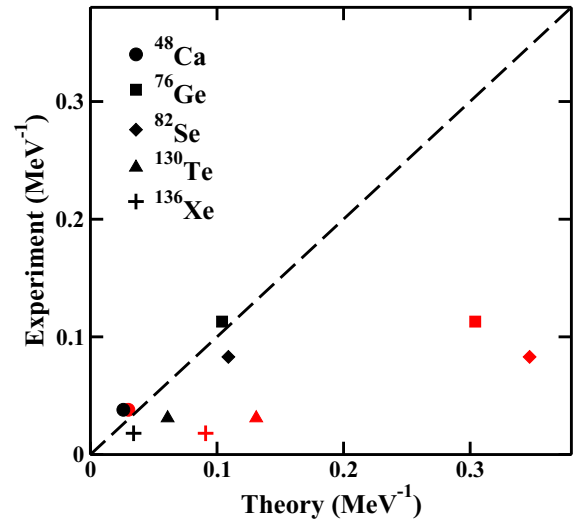


FIG. 15. Correlation plot between the calculated (x axis) and the experimental (y axis) $2\nu\beta\beta$ decay NMEs (see text for details).

effective spin-dependent operators is enlightened. Present work takes advantage of modern developments to derive the effective shell-model Hamiltonians and operators (see, for example, Refs. [3,6]), and up-to-date approaches to the renormalization of realistic NN potentials [41].

On the above grounds, we intend to extend our study by investigating the role of meson-exchange corrections to the electroweak currents [28–31]. More precisely, we aim, in the near future, at building up effective shell-model Hamiltonians and operators starting from two- and three-body nuclear potentials derived within the framework of chiral perturbation theory [77], and taking also into account the contributions of chiral two-body electroweak currents to the effective GT operators. As a matter of fact, recent studies have shown that β - and neutrinoless double- β decays may be significantly affected by these contributions [78,79], when consistently starting from chiral potentials.

At last, our final goal is to benefit from the expertise we have gained to evaluate the $0\nu\beta\beta$ decay NMEs for the nuclei studied in present paper [80].

APPENDIX: TABLES OF SP ENERGIES AND EFFECTIVE OPERATORS

1. SP energies

TABLE XI. Theoretical proton and neutron SP energy spacings (in MeV) for ^{40}Ca core.

	Proton SP spacings	Neutron SP spacings
$0f_{7/2}$	0.0	0.0
$0f_{5/2}$	8.6	7.8
$1p_{3/2}$	1.6	2.1
$1p_{1/2}$	3.3	4.0

TABLE XII. Theoretical proton and neutron SP energy spacings (in MeV) for ^{56}Ni core.

	Proton SP spacings	Neutron SP spacings
$0f_{5/2}$	0.2	0.0
$1p_{3/2}$	0.0	0.5
$1p_{1/2}$	0.6	1.1
$0g_{9/2}$	3.1	3.5

TABLE XIII. Theoretical proton and neutron SP energy spacings (in MeV) for ^{100}Sn core.

	Proton SP spacings	Neutron SP spacings
$0g_{7/2}$	0.0	0.0
$1d_{5/2}$	0.3	0.6
$1d_{3/2}$	1.2	1.5
$2s_{1/2}$	1.1	1.2
$0h_{11/2}$	1.9	2.7

2. Effective $M1$ and GT operators

TABLE XIV. Proton and neutron matrix elements of the effective magnetic dipole operator $M1$ (I) (in μ_N) for the ^{40}Ca core. In the last column we report the corresponding quenching factors. For l -forbidden matrix elements there is no quenching factor to be shown.

$n_a l_a j_a$ $n_b l_b j_b$	T_z	$M1_{\text{eff}}$	quenching factor
$0f_{7/2}$ $0f_{7/2}$	+1/2	8.760	0.965
$0f_{7/2}$ $0f_{5/2}$	+1/2	-3.986	0.961
$0f_{5/2}$ $0f_{7/2}$	+1/2	4.640	1.118
$0f_{5/2}$ $0f_{5/2}$	+1/2	1.310	1.073
$0f_{5/2}$ $1p_{3/2}$	+1/2	-0.017	
$1p_{3/2}$ $0f_{5/2}$	+1/2	0.014	
$1p_{3/2}$ $1p_{3/2}$	+1/2	4.462	0.933
$1p_{3/2}$ $1p_{1/2}$	+1/2	-2.396	0.926
$1p_{1/2}$ $1p_{3/2}$	+1/2	2.377	0.919
$1p_{1/2}$ $1p_{1/2}$	+1/2	-0.304	0.962
$0f_{7/2}$ $0f_{7/2}$	-1/2	-2.237	0.746
$0f_{7/2}$ $0f_{5/2}$	-1/2	3.308	0.956
$0f_{5/2}$ $0f_{7/2}$	-1/2	-3.582	1.035
$0f_{5/2}$ $0f_{5/2}$	-1/2	2.727	1.409
$0f_{5/2}$ $1p_{3/2}$	-1/2	-0.026	
$1p_{3/2}$ $0f_{5/2}$	-1/2	0.024	
$1p_{3/2}$ $1p_{3/2}$	-1/2	-2.074	0.859
$1p_{3/2}$ $1p_{1/2}$	-1/2	2.025	0.938
$1p_{1/2}$ $1p_{3/2}$	-1/2	-2.008	0.930
$1p_{1/2}$ $1p_{1/2}$	-1/2	0.799	1.047

TABLE XV. Same as in Table XIV, but for the ^{56}Ni core.

$n_a l_a j_a$ $n_b l_b j_b$	T_z	$M1_{\text{eff}}$	quenching factor
$0f_{5/2}$ $0f_{5/2}$	+1/2	2.212	1.812
$0f_{5/2}$ $1p_{3/2}$	+1/2	-0.033	
$1p_{3/2}$ $0f_{5/2}$	+1/2	0.026	
$1p_{3/2}$ $1p_{3/2}$	+1/2	3.358	0.739
$1p_{3/2}$ $1p_{1/2}$	+1/2	-1.554	0.601
$1p_{1/2}$ $1p_{3/2}$	+1/2	1.586	0.613
$1p_{1/2}$ $1p_{1/2}$	+1/2	-0.091	0.288
$0g_{9/2}$ $0g_{9/2}$	+1/2	10.174	0.877
$0f_{5/2}$ $0f_{5/2}$	-1/2	1.338	0.691
$0f_{5/2}$ $1p_{3/2}$	-1/2	-0.024	
$1p_{3/2}$ $0f_{5/2}$	-1/2	0.028	
$1p_{3/2}$ $1p_{3/2}$	-1/2	-1.233	0.511
$1p_{3/2}$ $1p_{1/2}$	-1/2	1.178	0.546
$1p_{1/2}$ $1p_{3/2}$	-1/2	-1.209	0.560
$1p_{1/2}$ $1p_{1/2}$	-1/2	0.512	0.671
$0g_{9/2}$ $0g_{9/2}$	-1/2	-0.473	0.145

TABLE XVI. Same as in Table XIV, but for the ^{100}Sn core.

$n_a l_a j_a$ $n_b l_b j_b$	T_z	$M1_{\text{eff}}$	quenching factor
$0g_{7/2}$ $0g_{7/2}$	+1/2	3.013	1.120
$0g_{7/2}$ $1d_{5/2}$	+1/2	-0.064	
$1d_{5/2}$ $0g_{7/2}$	+1/2	0.060	
$1d_{5/2}$ $1d_{5/2}$	+1/2	5.190	0.765
$1d_{5/2}$ $1d_{3/2}$	+1/2	-2.180	0.628
$1d_{3/2}$ $1d_{5/2}$	+1/2	2.274	0.655
$1d_{3/2}$ $1d_{3/2}$	+1/2	0.407	2.599
$1d_{3/2}$ $2s_{1/2}$	+1/2	-0.123	
$2s_{1/2}$ $1d_{3/2}$	+1/2	0.119	
$2s_{1/2}$ $2s_{1/2}$	+1/2	2.453	0.734
$0h_{11/2}$ $0h_{11/2}$	+1/2	12.349	0.861
$0g_{7/2}$ $0g_{7/2}$	-1/2	1.984	0.851
$0g_{7/2}$ $1d_{5/2}$	-1/2	-0.008	
$1d_{5/2}$ $0g_{7/2}$	-1/2	0.008	
$1d_{5/2}$ $1d_{5/2}$	-1/2	-1.417	0.523
$1d_{5/2}$ $1d_{3/2}$	-1/2	1.681	0.580
$1d_{3/2}$ $1d_{5/2}$	-1/2	-1.756	0.606
$1d_{3/2}$ $1d_{3/2}$	-1/2	1.081	0.746
$1d_{3/2}$ $2s_{1/2}$	-1/2	0.076	
$2s_{1/2}$ $1d_{3/2}$	-1/2	-0.071	
$2s_{1/2}$ $2s_{1/2}$	-1/2	-1.414	0.618
$0h_{11/2}$ $0h_{11/2}$	-1/2	-0.696	0.198

TABLE XVII. Matrix elements of the proton-neutron effective GT^+ and GT^- operators for the ^{40}Ca core. In the last two columns we report the corresponding quenching factors of the present work (I) and those reported in the work of Ref. [7] (see text for details). For l -forbidden matrix elements there is no quenching factor to be shown.

$n_a l_a j_a n_b l_b j_b$	GT_{eff}^-	quenching factor	
$0f_{7/2} 0f_{7/2}$	2.870	0.995	
$0f_{7/2} 0f_{5/2}$	-3.210	0.964	
$0f_{5/2} 0f_{7/2}$	3.941	1.183	
$0f_{5/2} 0f_{5/2}$	-2.104	1.130	
$0f_{5/2} 1p_{3/2}$	-0.033		
$1p_{3/2} 0f_{5/2}$	0.001		
$1p_{3/2} 1p_{3/2}$	2.162	0.931	
$1p_{3/2} 1p_{1/2}$	-1.906	0.918	
$1p_{1/2} 1p_{3/2}$	1.901	0.915	
$1p_{1/2} 1p_{1/2}$	-0.691	0.953	
$n_a l_a j_a n_b l_b j_b$	GT_{eff}^+	quenching factor (I)	quenching factor (II)
$0f_{7/2} 0f_{7/2}$	2.706	0.938	0.905
$0f_{7/2} 0f_{5/2}$	-3.012	0.904	0.856
$0f_{5/2} 0f_{7/2}$	3.276	0.984	
$0f_{5/2} 0f_{5/2}$	-1.737	0.932	0.882
$0f_{5/2} 1p_{3/2}$	-0.001		
$1p_{3/2} 0f_{5/2}$	0.026		
$1p_{3/2} 1p_{3/2}$	2.135	0.921	0.880
$1p_{3/2} 1p_{1/2}$	-1.879	0.904	0.863
$1p_{1/2} 1p_{3/2}$	1.871	0.901	
$1p_{1/2} 1p_{1/2}$	-0.686	0.935	0.932

TABLE XVIII. Same as in Table XVII, but for the ^{56}Ni core.

$n_a l_a j_a n_b l_b j_b$	GT_{eff}^-	quenching factor	
$0f_{5/2} 0f_{5/2}$	-0.674	0.362	
$0f_{5/2} 1p_{3/2}$	-0.085		
$1p_{3/2} 0f_{5/2}$	0.006		
$1p_{3/2} 1p_{3/2}$	1.441	0.620	
$1p_{3/2} 1p_{1/2}$	-1.141	0.549	
$1p_{1/2} 1p_{3/2}$	1.189	0.572	
$1p_{1/2} 1p_{1/2}$	-0.482	0.657	
$0g_{9/2} 0g_{9/2}$	1.608	0.511	
$n_a l_a j_a n_b l_b j_b$	GT_{eff}^+	quenching factor (I)	quenching factor (II)
$0f_{5/2} 0f_{5/2}$	-0.638	0.342	0.458
$0f_{5/2} 1p_{3/2}$	-0.011		
$1p_{3/2} 0f_{5/2}$	0.061		
$1p_{3/2} 1p_{3/2}$	1.405	0.605	0.689
$1p_{3/2} 1p_{1/2}$	-1.159	0.558	0.680
$1p_{1/2} 1p_{3/2}$	1.121	0.539	
$1p_{1/2} 1p_{1/2}$	-0.468	0.638	
$0g_{9/2} 0g_{9/2}$	1.536	0.488	0.802

TABLE XIX. Same as in Table XVII, but for the ^{100}Sn core.

$n_a l_a j_a n_b l_b j_b$	GT_{eff}^-	quenching factor	
$0g_{7/2} 0g_{7/2}$	-1.168	0.521	
$0g_{7/2} 1d_{5/2}$	-0.108		
$1d_{5/2} 0g_{7/2}$	0.000		
$1d_{5/2} 1d_{5/2}$	1.686	0.647	
$1d_{5/2} 1d_{3/2}$	-1.525	0.547	
$1d_{3/2} 1d_{5/2}$	1.708	0.613	
$1d_{3/2} 1d_{3/2}$	-0.888	0.638	
$1d_{3/2} 2s_{1/2}$	-0.124		
$2s_{1/2} 1d_{3/2}$	0.093		
$2s_{1/2} 2s_{1/2}$	1.405	0.638	
$0h_{11/2} 0h_{11/2}$	1.931	0.570	
$n_a l_a j_a n_b l_b j_b$	GT_{eff}^+	quenching factor (I)	quenching factor (II)
$0g_{7/2} 0g_{7/2}$	-1.168	0.521	0.472
$0g_{7/2} 1d_{5/2}$	0.001		
$1d_{5/2} 0g_{7/2}$	0.102		
$1d_{5/2} 1d_{5/2}$	1.686	0.647	0.595
$1d_{5/2} 1d_{3/2}$	-1.688	0.606	0.513
$1d_{3/2} 1d_{5/2}$	1.543	0.553	
$1d_{3/2} 1d_{3/2}$	-0.888	0.638	0.652
$1d_{3/2} 2s_{1/2}$	-0.098		
$2s_{1/2} 1d_{3/2}$	0.117		
$2s_{1/2} 2s_{1/2}$	1.405	0.638	
$0h_{11/2} 0h_{11/2}$	1.931	0.570	

- [1] *Lecture Notes in Physics*, Vol. 936, edited by M. Hjorth-Jensen, M. P. Lombardo, and U. van Kolck (Springer, Berlin, 2017).
- [2] M. Hjorth-Jensen, T. T. S. Kuo, and E. Osnes, *Phys. Rep.* **261**, 125 (1995).
- [3] L. Coraggio, A. Covello, A. Gargano, N. Itaco, and T. T. S. Kuo, *Ann. Phys. (NY)* **327**, 2125 (2012).
- [4] L. Coraggio, A. Covello, A. Gargano, N. Itaco, and T. T. S. Kuo, *Prog. Part. Nucl. Phys.* **62**, 135 (2009).
- [5] P. J. Ellis and E. Osnes, *Rev. Mod. Phys.* **49**, 777 (1977).
- [6] K. Suzuki and R. Okamoto, *Prog. Theor. Phys.* **93**, 905 (1995).
- [7] T. Siiskonen, M. Hjorth-Jensen, and J. Suhonen, *Phys. Rev. C* **63**, 055501 (2001).
- [8] J. D. Holt and J. Engel, *Phys. Rev. C* **87**, 064315 (2013).
- [9] J. Barea and F. Iachello, *Phys. Rev. C* **79**, 044301 (2009).
- [10] J. Barea, J. Kotila, and F. Iachello, *Phys. Rev. Lett.* **109**, 042501 (2012).
- [11] J. Barea, J. Kotila, and F. Iachello, *Phys. Rev. C* **87**, 014315 (2013).
- [12] F. Šimkovic, A. Faessler, V. Rodin, P. Vogel, and J. Engel, *Phys. Rev. C* **77**, 045503 (2008).
- [13] F. Šimkovic, A. Faessler, H. Mütter, V. Rodin, and M. Stauf, *Phys. Rev. C* **79**, 055501 (2009).
- [14] D.-L. Fang, A. Faessler, V. Rodin, and F. Šimkovic, *Phys. Rev. C* **83**, 034320 (2011).
- [15] A. Faessler, V. Rodin, and F. Šimkovic, *J. Phys. G* **39**, 124006 (2012).
- [16] F. Šimkovic, A. Smetana, and P. Vogel, *Phys. Rev. C* **98**, 064325 (2018).
- [17] E. Caurier, F. Nowacki, and A. Poves, *Eur. Phys. J. A* **36**, 195 (2008).
- [18] J. Menéndez, A. Poves, E. Caurier, and F. Nowacki, *Phys. Rev. C* **80**, 048501 (2009).
- [19] J. Menéndez, A. Poves, E. Caurier, and F. Nowacki, *Nucl. Phys. A* **818**, 139 (2009).
- [20] E. Caurier, F. Nowacki, and A. Poves, *Phys. Lett. B* **711**, 62 (2012).
- [21] M. Horoi, S. Stoica, and B. A. Brown, *Phys. Rev. C* **75**, 034303 (2007).
- [22] M. Horoi, *Phys. Rev. C* **87**, 014320 (2013).
- [23] M. Horoi and B. A. Brown, *Phys. Rev. Lett.* **110**, 222502 (2013).
- [24] A. Neacsu and M. Horoi, *Phys. Rev. C* **91**, 024309 (2015).
- [25] B. A. Brown, D. L. Fang, and M. Horoi, *Phys. Rev. C* **92**, 041301(R) (2015).
- [26] Y. Iwata, N. Shimizu, T. Otsuka, Y. Utsuno, J. Menéndez, M. Honma, and T. Abe, *Phys. Rev. Lett.* **116**, 112502 (2016).
- [27] J. T. Suhonen, *Front. Phys.* **55**, 5 (2017).
- [28] T. S. Park, D. P. Min, and M. Rho, *Phys. Rep.* **233**, 341 (1993).
- [29] S. Pastore, L. Girlanda, R. Schiavilla, M. Viviani, and R. B. Wiringa, *Phys. Rev. C* **80**, 034004 (2009).
- [30] M. Piarulli, L. Girlanda, L. E. Marcucci, S. Pastore, R. Schiavilla, and M. Viviani, *Phys. Rev. C* **87**, 014006 (2013).
- [31] A. Baroni, L. Girlanda, S. Pastore, R. Schiavilla, and M. Viviani, *Phys. Rev. C* **93**, 015501 (2016).
- [32] M. Tanabashi, K. Hagiwara, K. Hikasa, K. Nakamura, Y. Sumino, F. Takahashi, J. Tanaka, K. Agashe, G. Aielli,

- C. Amsler *et al.* (Particle Data Group), *Phys. Rev. D* **98**, 030001 (2018).
- [33] I. S. Towner, *Phys. Rep.* **155**, 263 (1987).
- [34] I. S. Towner and K. F. C. Khanna, *Nucl. Phys. A* **399**, 334 (1983).
- [35] J. Suhonen, *Phys. Rev. C* **96**, 055501 (2017).
- [36] A. Baroni, L. Girlanda, A. Kievsky, L. E. Marcucci, R. Schiavilla, and M. Viviani, *Phys. Rev. C* **94**, 024003 (2016).
- [37] T. T. S. Kuo, J. Shurpin, K. C. Tam, E. Osnes, and P. J. Ellis, *Ann. Phys. (NY)* **132**, 237 (1981).
- [38] L. Coraggio, L. De Angelis, T. Fukui, A. Gargano, and N. Itaco, *Phys. Rev. C* **95**, 064324 (2017).
- [39] R. Machleidt, *Phys. Rev. C* **63**, 024001 (2001).
- [40] S. Bogner, T. T. S. Kuo, and L. Coraggio, *Nucl. Phys. A* **684**, 432c (2001).
- [41] S. Bogner, T. T. S. Kuo, L. Coraggio, A. Covello, and N. Itaco, *Phys. Rev. C* **65**, 051301(R) (2002).
- [42] L. Coraggio, A. Covello, A. Gargano, N. Itaco, and T. T. S. Kuo, *Phys. Rev. C* **91**, 041301(R) (2015).
- [43] L. Coraggio, A. Gargano, and N. Itaco, *JPS Conf. Proc.* **6**, 020046 (2015).
- [44] L. Coraggio, A. Gargano, and N. Itaco, *Phys. Rev. C* **93**, 064328 (2016).
- [45] T. T. S. Kuo and E. Osnes, *Lecture Notes in Physics*, Vol. 364 (Springer-Verlag, Berlin, 1990).
- [46] T. T. S. Kuo, F. Krmpotić, K. Suzuki, and R. Okamoto, *Nucl. Phys. A* **582**, 205 (1995).
- [47] T. T. S. Kuo, S. Y. Lee, and K. F. Ratcliff, *Nucl. Phys. A* **176**, 65 (1971).
- [48] L. Coraggio, A. Covello, A. Gargano, and N. Itaco, *Phys. Rev. C* **81**, 064303 (2010).
- [49] B. H. Brandow, *Rev. Mod. Phys.* **39**, 771 (1967).
- [50] E. M. Krenciglowa and T. T. S. Kuo, *Nucl. Phys. A* **235**, 171 (1974).
- [51] See Supplemental material at <http://link.aps.org/supplemental/10.1103/PhysRevC.100.014316> for the list of two-body matrix elements of the shell-model Hamiltonian H_{eff} .
- [52] L. Coraggio, L. De Angelis, T. Fukui, A. Gargano, and N. Itaco, *J. Phys. Conf. Ser.* **1056**, 012012 (2018).
- [53] G. A. Baker and J. L. Gammel, *The Padé Approximant in Theoretical Physics*, Vol. 71 of Mathematics in Science and Engineering (Academic Press, New York, 1970).
- [54] H. M. Hoffmann, Y. Starkand, and M. W. Kirson, *Nucl. Phys. A* **266**, 138 (1976).
- [55] C. D. Goodman, C. A. Goulding, M. B. Greenfield, J. Rapaport, D. E. Bainum, C. C. Foster, W. G. Love, and F. Petrovich, *Phys. Rev. Lett.* **44**, 1755 (1980).
- [56] T. N. Taddeucci, C. A. Goulding, T. A. Carey, R. C. Byrd, C. D. Goodman, C. Gaarde, J. Larsen, D. Horen, J. Rapaport, and E. Sugarbaker, *Nucl. Phys. A* **469**, 125 (1987).
- [57] E. Caurier, G. Martínez-Pinedo, F. Nowack, A. Poves, and A. P. Zuker, *Rev. Mod. Phys.* **77**, 427 (2005).
- [58] W. C. Haxton and G. J. Stephenson, Jr., *Prog. Part. Nucl. Phys.* **12**, 409 (1984).
- [59] R. A. Sen'kov and M. Horoi, *Phys. Rev. C* **88**, 064312 (2013).
- [60] M. Horoi, *J. Phys. Conf. Ser.* **413**, 012020 (2013).
- [61] A. S. Barabash, *Nucl. Phys. A* **935**, 52 (2015).
- [62] Data extracted using the NNDC On-line Data Service from the ENSDF database, file revised as of November 6, 2018, <https://www.nndc.bnl.gov/ensdf>
- [63] Data extracted using the NNDC On-line Data Service from the XUNDL database, file revised as of November 6, 2018, <https://www.nndc.bnl.gov/ensdf/ensdf/xundl.jsp>
- [64] J. R. Vanhoy, M. T. McEllistrem, S. F. Hicks, R. A. Gatenby, E. M. Baum, E. L. Johnson, G. Molnár, and S. W. Yates, *Phys. Rev. C* **45**, 1628 (1992).
- [65] K. Yako, M. Sasano, K. Miki, H. Sakai, M. Dozono, D. Frekers, M. B. Greenfield, K. Hatanaka, E. Ihara, M. Kato *et al.*, *Phys. Rev. Lett.* **103**, 012503 (2009).
- [66] S. Mukhopadhyay, B. P. Crider, B. A. Brown, S. F. Ashley, A. Chakraborty, A. Kumar, M. T. McEllistrem, E. E. Peters, F. M. Prados-Estévez, and S. W. Yates, *Phys. Rev. C* **95**, 014327 (2017).
- [67] G. Gürdal, E. A. Stefanova, P. Boutachkov, D. A. Torres, G. J. Kumbartzki, N. Benczer-Koller, Y. Y. Sharon, L. Zamick, S. J. Q. Robinson, T. Ahn *et al.*, *Phys. Rev. C* **88**, 014301 (2013).
- [68] K.-H. Speidel, N. Benczer-Koller, G. Kumbartzki, C. Barton, A. Gelberg, J. Holden, G. Jakob, N. Matt, R. H. Mayer, M. Satteson *et al.*, *Phys. Rev. C* **57**, 2181 (1998).
- [69] J. H. Thies, D. Frekers, T. Adachi, M. Dozono, H. Ejiri, H. Fujita, Y. Fujita, M. Fujiwara, E.-W. Grewe, K. Hatanaka *et al.*, *Phys. Rev. C* **86**, 014304 (2012).
- [70] D. Frekers, M. Alanssari, T. Adachi, B. T. Cleveland, M. Dozono, H. Ejiri, S. R. Elliott, H. Fujita, Y. Fujita, M. Fujiwara *et al.*, *Phys. Rev. C* **94**, 014614 (2016).
- [71] S. F. Hicks, J. R. Vanhoy, and S. W. Yates, *Phys. Rev. C* **78**, 054320 (2008).
- [72] P. Puppe, A. Lennarz, T. Adachi, H. Akimune, H. Ejiri, D. Frekers, H. Fujita, Y. Fujita, M. Fujiwara, E. Ganioglu, E.-W. Grewe, K. Hatanaka, R. Hodak, C. Iwamoto, N. T. Khai, A. Okamoto, H. Okamura, P. P. Povinec, G. Susoy, T. Suzuki, A. Tamii, J. H. Thies, and M. Yosoi, *Phys. Rev. C* **86**, 044603 (2012).
- [73] S. Mukhopadhyay, M. Scheck, B. Crider, S. N. Choudry, E. Elhami, E. Peters, M. T. McEllistrem, J. N. Orce, and S. W. Yates, *Phys. Rev. C* **78**, 034317 (2008).
- [74] D. Frekers, P. Puppe, J. H. Thies, and H. Ejiri, *Nucl. Phys. A* **916**, 219 (2013).
- [75] I. P. Johnstone and I. S. Towner, *Eur. Phys. J. A* **3**, 237 (1998).
- [76] B. A. Brown, N. J. Stone, J. R. Stone, I. S. Towner, and M. Hjorth-Jensen, *Phys. Rev. C* **71**, 044317 (2005).
- [77] T. Fukui, L. De Angelis, Y. Z. Ma, L. Coraggio, A. Gargano, N. Itaco, and F. R. Xu, *Phys. Rev. C* **98**, 044305 (2018).
- [78] J. Menéndez, D. Gazit, and A. Schwenk, *Phys. Rev. Lett.* **107**, 062501 (2011).
- [79] L.-J. Wang, J. Engel, and J. M. Yao, *Phys. Rev. C* **98**, 031301(R) (2018).
- [80] L. Coraggio, A. Gargano, N. Itaco, and F. Nowacki (unpublished).